nature nanotechnology

ARTICLES

https://doi.org/10.1038/s41565-020-00787-y

Check for updates

All-solid-state spatial light modulator with independent phase and amplitude control for three-dimensional LiDAR applications

Junghyun Park[1,6]✉, Byung Gil Jeong[1,6], Sun Il Kim[1,6], Duhyun Lee[1], Jungwoo Kim[1], Changgyun Shin[1], Chang Bum Lee[1], Tatsuhiro Otsuka[1], Jisoo Kyoung[1,5], Sangwook Kim[1], Ki-Yeon Yang[1], Yong-Young Park[1], Jisan Lee[1], Inoh Hwang[1], Jaeduck Jang[1], Seok Ho Song[2], Mark L. Brongersma[3], Kyoungho Ha[1], Sung-Woo Hwang[1], Hyuck Choo[1]✉ and Byoung Lyong Choi[4]✉

Spatial light modulators are essential optical elements in applications that require the ability to regulate the amplitude, phase and polarization of light, such as digital holography, optical communications and biomedical imaging. With the push towards miniaturization of optical components, static metasurfaces are used as competent alternatives. These evolved to active metasurfaces in which light-wavefront manipulation can be done in a time-dependent fashion. The active metasurfaces reported so far, however, still show incomplete phase modulation (below 360°). Here we present an all-solid-state, electrically tunable and reflective metasurface array that can generate a specific phase or a continuous sweep between 0 and 360° at an estimated rate of 5.4 MHz while independently adjusting the amplitude. The metasurface features 550 individually addressable nanoresonators in a 250 × 250 μm² area with no micromechanical elements or liquid crystals. A key feature of our design is the presence of two independent control parameters (top and bottom gate voltages) in each nanoresonator, which are used to adjust the real and imaginary parts of the reflection coefficient independently. To demonstrate this array's use in light detection and ranging, we performed a three-dimensional depth scan of an emulated street scene that consisted of a model car and a human figure up to a distance of 4.7 m.

Spatial light modulators (SLMs) regulate the amplitude, phase and polarization of light and serve as the core components of many optical applications, such as digital holographic systems, optical communication modules and biomedical imaging systems[1–4]. The recent emergence of new applications, such as wearable displays for augmented reality or light detection and ranging (LiDAR) sensors for autonomous vehicles, demands the development of new SLMs with an improved field of view, speed and reliability compared with those of the conventional devices that rely on liquid crystals[5,6] and microelectromechanical systems[7,8].

To meet this demand, the use of active metasurfaces has been explored[9]. Metasurfaces were first investigated as assemblies of passive, static nanoscale optical elements that provided control over the amplitude, phase and polarization of transmitted or reflected light[10–14], and then evolved into active metasurfaces that could enable ultrafast wavefront manipulation and a wide field of view in a compact form factor[15]. Pioneering studies exploited various tunable materials and designs, which included transparent conducting oxides[16–19], phase-change materials[20–22], semiconductors[23,24], two-dimensional (2D) materials[25–28], micromechanical actuators[29], frequency-gradient sources[30] and liquid crystals[6].

The active metasurfaces reported to date, however, show incomplete phase modulation below 360° and undesired cross-modulation of the amplitude and phase. This limitation mainly arises from the use of a single control parameter to modulate 2D phenomena, such as transmission or reflection described by complex coefficients that consist of real (r_{real}) and imaginary (r_{imag}) parts[9–13]. Complex modulation is a 2D phenomenon, and its control requires the use of two control parameters. This intuitive principle can be verified for most of the passive metasurfaces that successfully demonstrate static wavefront manipulation because these metasurfaces exploit at least two in-plane geometric parameters, such as the width and length or the orientation angle and diameter[11–13,31,32]. To extend the phase modulation range, a recent study reported the use of dual gates in which two identical or opposite voltages were applied; by this approach, a modulation of 300° was reported[19] (Supplementary Section 1 and Supplementary Fig. 1).

Here we present an all-solid-state SLM composed of an electrically tunable metasurface array (Fig. 1a) designed to demonstrate the two-control-parameter approach in the near infrared (NIR) regime. The array consists of plasmonic nanoresonators whose reflection coefficient can be tuned by applying separate electrical biases V_t and V_b to the top and bottom electrodes of the nanoresonators (Fig. 1b). Detailed numerical and experimental investigations revealed that a careful selection of the operating ranges for V_t and V_b allowed us to assign one of the two voltages to adjust the real part of the reflection coefficient (r), whereas the other voltage was used to control the imaginary part. Utilizing V_t and V_b as two separate control knobs, we achieved a completely independent control of the amplitude and phase over 360° and demonstrated an increased

[1]Samsung Advanced Institute of Technology, Samsung Electronics, Suwon, Republic of Korea. [2]Department of Physics, Hanyang University, Seoul, Republic of Korea. [3]Geballe Lab for Advanced Materials, Stanford University, Stanford, CA, USA. [4]School of Advanced Materials Science and Engineering, Sungkyunkwan University, Suwon, Republic of Korea. [5]Present address: Department of Physics, Dankook University, Cheonan, Republic of Korea. [6]These authors contributed equally: Junghyun Park, Byung Gil Jeong, Sun Il Kim. ✉e-mail: jhy.park@samsung.com; hyuck.choo@samsung.com; choibl@skku.edu

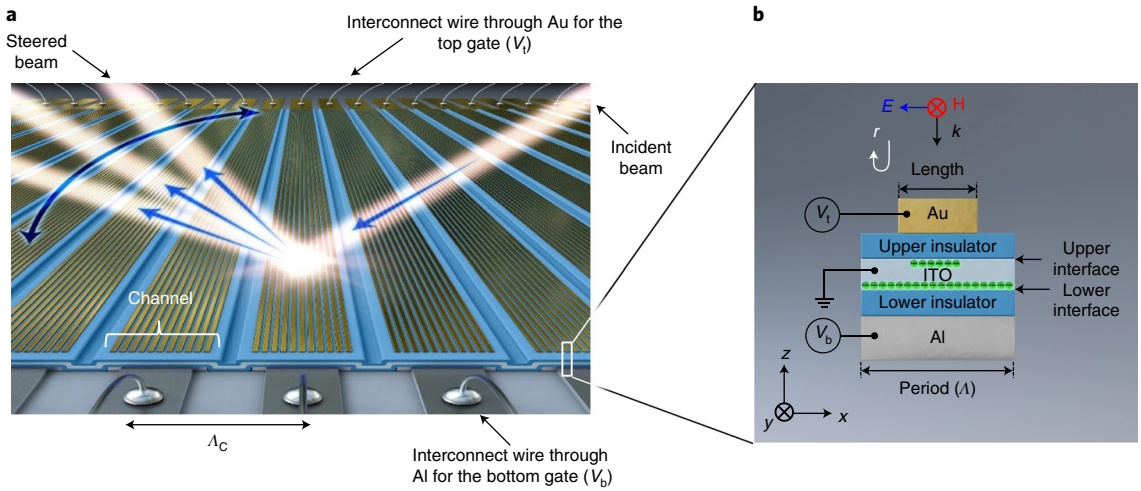

Fig. 1 | All-solid-state active metasurface based on the two-control-parameter approach. a, Illustration of the active metasurface array composed of electrically tunable channels, with each channel composed of 11 individually addressable plasmonic nanoresonators. The incident beam on the top right is reflected from the metasurface array, and the direction of the steered beam is controlled by adjusting the top and bottom gates, V_t and V_b, respectively. The channel period is denoted by Λ_C. **b**, Cross-sectional view of a single plasmonic nanoresonator showing the top Au nanoantenna, the active ITO layer in the middle and the bottom Al mirror. The upper and lower insulators electrically isolate the three structures from one another, which keeps the ITO layer grounded and allows the top Au nanoantenna and the bottom Al mirror to serve as the top (V_t) and bottom (V_b) electrodes, respectively.

degree of freedom in the modulation of the reflection coefficient. In addition to performing phase-only modulation, versatile beam splitting and steering, we demonstrate the use of the active metasurface as a solid-state scanner in a LiDAR system to generate a 3D range map.

Two-control parameter for independent phase-amplitude control

To demonstrate the two-control-parameter approach, we fabricated an array of tunable plasmonic nanoresonators (Fig. 1a), with each consisting of a Au nanoantenna on top, an indium tin oxide (ITO) layer in the middle and an Al mirror on the bottom (Fig. 1b). These three structures were electrically isolated from one another by two oxide layers on the top and bottom of the ITO layer (Fig. 1b). The Au nanoantenna and the Al mirror served as separate top and bottom electrodes.

We modelled the nanoresonator with an Al mirror on the bottom (Fig. 1) as a one-port resonator and obtained its reflection coefficient r by using the temporal coupled mode theory[33]:

$$r = r_{\mathrm{real}} + ir_{\mathrm{imag}} = \frac{(\gamma_{\mathrm{rad}} - \gamma_{\mathrm{abs}}) - i(\omega_s - \omega_r)}{(\gamma_{\mathrm{rad}} + \gamma_{\mathrm{abs}}) + i(\omega_s - \omega_r)} \quad (1)$$

where ω_r is the resonance angular frequency ($=2\pi c_0/\lambda_r$), c_0 is the speed of light, λ_r is the resonance wavelength and ω_s is the angular frequency of the light source ($=2\pi c_0/\lambda_s$). γ_{rad} and γ_{abs} are the decay rates due to the external radiation and internal optical loss, respectively.

While the value γ_{rad} is essentially fixed, the other two variables ω_r and γ_{abs} can be adjusted electrically. By judiciously selecting and independently applying the appropriate V_t and V_b, we could form charge-accumulation or -depletion layers at the upper and lower interfaces between the ITO layer and the insulating oxide layers (Fig. 1b). This influences ω_r and γ_{abs} and changes r_{imag} and r_{real} to produce the desired reflection coefficient.

To elucidate how the applied biases can adjust the accumulation and depletion layers and influence r, we chose the values for γ_{rad}, γ_{abs}, ω_s and ω_r in equation (1) such that the plasmonic nanoresonator had the resonance at 1.3 μm ($\omega_s = \omega_r = 2\pi c_0/(1.3\,\mu\mathrm{m})$) and was in the critically coupled regime ($\gamma_{\mathrm{rad}} = \gamma_{\mathrm{abs}}$) with no applied bias (Methods). We plot the reflectivity $|r|^2$ and phase in Fig. 2a,b, respectively, in which no-bias cases are presented with green curves. The reflection dip occurs at the wavelength of 1.3 μm (Fig. 2a) and the phase plot shows an abrupt change due to the singularity (Fig. 2b). Figure 2c shows the resulting reflection coefficients in the complex r plane, where the circles depict the spectral evolution of the reflection coefficients and the green diamond corresponds to the reflection coefficient at the wavelength of 1.3 μm.

If the applied V_t and V_b are positive with respect to the grounded ITO, accumulation layers form at the interfaces between the ITO and the oxide layers, and the plasma frequency increases (Supplementary Section 2 and Supplementary Fig. 2). The increase in the plasma frequency decreases the real part of the dielectric constant inside the ITO layer ($\varepsilon_{\mathrm{ITO}}$) (Supplementary Section 3) and reduces the effective mode index of the gap plasmon, which causes a blueshift of the resonance (blue curve in Fig. 2a), that is $\lambda_r < \lambda_s$ ($\omega_r > \omega_s$). In addition, the internal optical loss γ_{abs} also increases because the magnitude of the imaginary part of $\varepsilon_{\mathrm{ITO}}$ increases. Consequently, the coupling dynamics for the plasmonic nanoresonator shifts towards the undercoupled regime denoted by the dark grey circle (Fig. 2c), that is, $\gamma_{\mathrm{rad}} < \gamma_{\mathrm{abs}}$ (ref. [18]), and this typically has a stronger effect on r_{real} than on r_{imag}. (Supplementary Section 4, Supplementary Figs. 3–5 and Supplementary Movie 1). The vector sum of the changes in r_{real} and r_{imag} results in an anticlockwise vector movement denoted by the blue arrow in Fig. 2c.

Similarly, if V_t and V_b are negative with respect to the grounded ITO, depletion layers are formed at the interfaces, which generates a redshift (red curve in Fig. 2a), that is, $\lambda_r > \lambda_s$ ($\omega_r < \omega_s$), and decreases the internal loss. In this case, the nanoresonator is in the overcoupled regime denoted by the light grey circle ($\gamma_{\mathrm{rad}} > \gamma_{\mathrm{abs}}$) (Fig. 2c) and this mostly influences r_{imag} (Supplementary Section 4, Supplementary Figs. 3–5 and Supplementary Movie 2). The changes in r_{imag} and r_{real} lead to the downward-pointing, clockwise vector movement denoted by the red arrow in Fig. 2c.

We conducted full-field simulations to explain the tuning range of r more quantitatively by varying V_t from −4 to 4 V and V_b from −6.4 to 6.4 V (Fig. 2d and Methods). The resulting r values are shown in Fig. 2e. The design of the nanoresonators and the ranges of

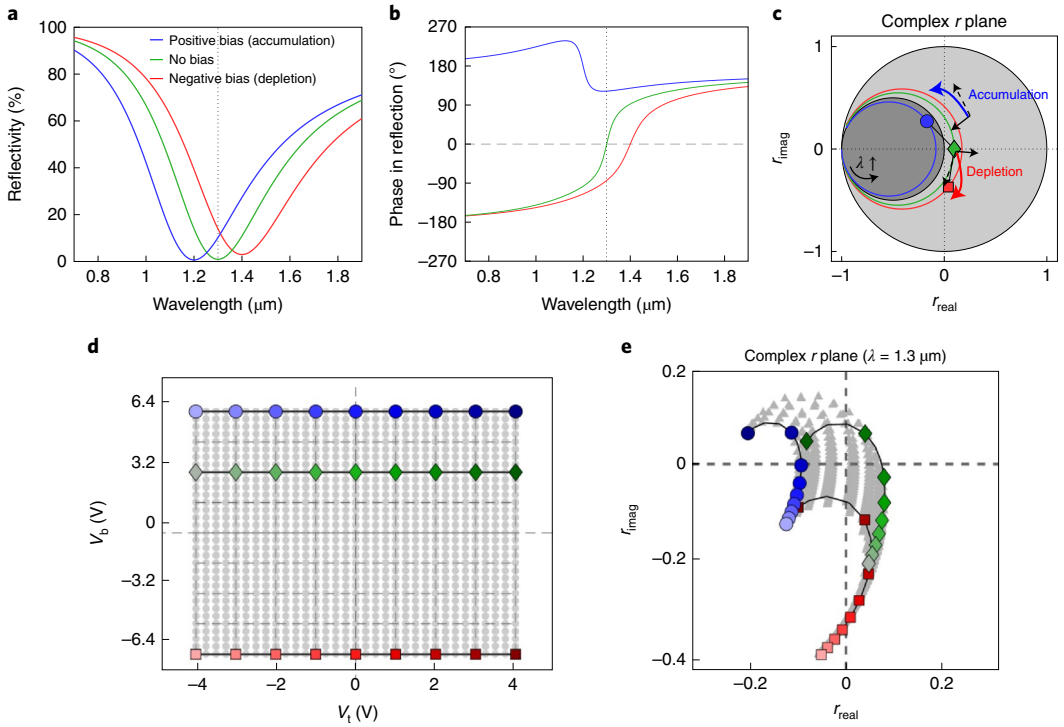

Fig. 2 | Two-control-parameter approach for full wavefront modulation: simulations of the relationship between (V_t, V_b) and r. a, Reflection spectra showing resonance shifts caused by positive (accumulation, undercoupled) and negative (depletion, overcoupled) biases. **b**, Reflection-phase spectra showing the transition of the coupling dynamics caused by positive and negative biases. **c**, Complex reflection coefficients r for the range of the wavelengths from 0.7 to 1.9 μm represented by green, blue and red symbols under zero (near-critically coupled), positive and negative biases, respectively. Green diamond (no bias), blue circle (positive) and red square (negative) represent the coefficients for the wavelength of 1.3 μm. Dark and light grey circles denote the range of complex coefficients in the under- and overcoupled regimes, respectively. **d**, Voltage combinations (V_t, V_b) marked by grey and coloured symbols. **e**, The reflection coefficients, which result from applying the voltage combinations shown in **d**, were obtained by carrying out full-field simulations (Supplementary Movie 3) and are denoted by the corresponding grey and coloured symbols. The voltage combinations can generate any coefficients on and around the origin, which implies an independent modulation of the amplitude and phase over 360°.

V_t and V_b were selected such that the resulting set of r values centred around the origin and it covered all four quadrants of the complex r plane so as to provide a continuous 0–360° phase change. This set of r values provided a relatively low reflectivity for staying close to the origin. However, the benefit of having the complete phase-shifting range and the independent, fine amplitude modulation outweighed the decrease in reflectivity and substantially improved the overall wavefront-modulation quality with a high side mode suppression ratio (SMSR) (Supplementary Section 5 and Supplementary Figs. 6 and 7).

Three similar trajectories roughly define the outer boundaries of the tunable range in Fig. 2e. Each position is mainly determined by the different value of V_b, which were set to −6.4 (red dots), 3.2 (green dots) or 6.4 V (blue dots). In all three cases, as V_t increased from −4 V, the trajectory initially moved upward; the device was dominated by depletion in the overcoupled regime and changes occurred mostly in r_{imag}. When V_t increased beyond 3 V, the upward motion sharply changed to a lateral motion; the device was dominated by accumulation in the undercoupled regime and changes were greater for r_{real}, which resulted in a hook-shaped trajectory in the phasor diagram (Fig. 2e). A careful selection of the operating ranges for V_t and V_b allowed one of the voltages to adjust r_{real} and the other to modify r_{imag}. Owing to the structural symmetry, the roles of V_t and V_b were completely interchangeable (Supplementary Section 6 and Supplementary Fig. 8).

Varying V_t only and fixing V_b at −6.4, 3.2 or 6.4 V, we obtained the single-control-parameter case with only a single hook-shaped trajectory of the reflection coefficients. As we activated the other degree of freedom, that is, independently varied V_b within the given range, we observed a translation (offset) of the hook without a substantial shape alteration, which provided the 2D areal coverage of the achievable reflection coefficients (Fig. 2e and Supplementary Movie 3). Owing to the two degrees of freedom in control, the vector changes in reflection phasors caused by the two applied biases could be independently superposed to achieve an excellent wavefront control (Extended Data Figs. 1 and 2).

To demonstrate the generation of on-demand reflection coefficients, we targeted 13 different reflection coefficients (Fig. 3). Figure 3a–c elucidates the electric field distribution for three different voltage combinations to yield points I, II and III in Fig. 3d. First, to generate $r_{target} = 0.08i$ at I, we started from the reflection coefficient (the second darkest green dot) in Fig. 2e that corresponds to (V_t, V_b) = (3.00 V, 3.20 V). We slightly increased V_t to 3.25 V to enhance the accumulation and bring the coefficient closer to the imaginary axis. We observed a strong intensity enhancement $|E_x|^2 + |E_z|^2$ (left inset of Fig. 3a), whereas a strong charge accumulation and vanishing $\mathrm{Re}(\varepsilon_{ITO})$ at both the upper and lower interfaces are shown in the right insets. This produced an r of $0.0034 + 0.0815i$.

To generate $r_{target} = 0$ at II, we decreased r_{imag} by lowering V_t to 0.50 V and removing the enhancement and the accumulation layer at the upper interface (Fig. 3b insets). This caused an increase of $\mathrm{Re}(\varepsilon_{ITO})$ at the upper interface, a redshift of the resonance and thus a decrease in r_{imag}. To compensate for the decreased internal optical loss, we increased V_b from 3.20 to 4.65 V to yield a coefficient of $0.0003 + 0.0026i$. The field distribution (Fig. 3b) shows an almost identical phase to that of Fig. 3a as the amplitude becomes almost zero.

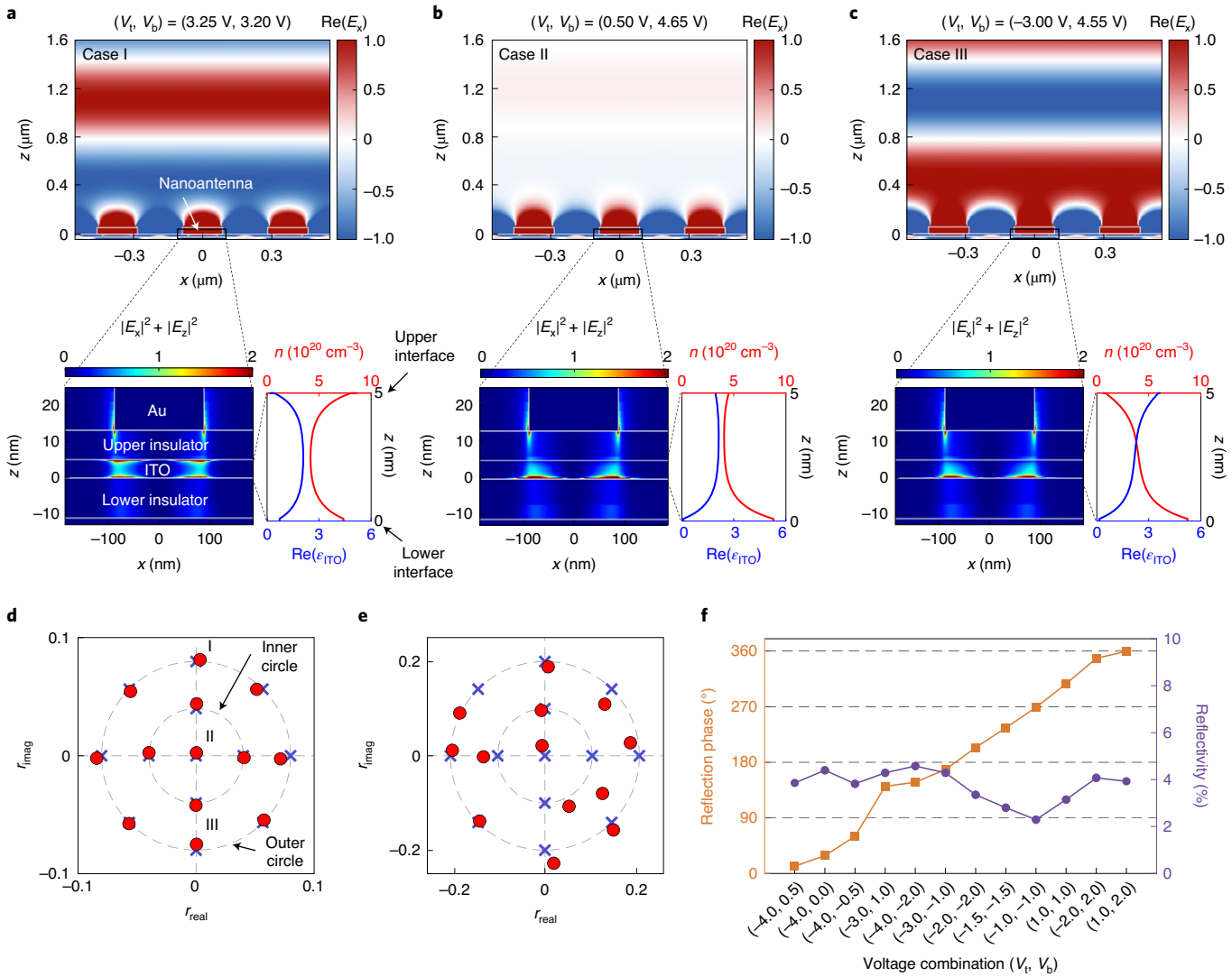

Fig. 3 | Targeting specific reflection coefficients distributed on the constellation diagram by using the proposed two-control-parameter approach. **a**–**c**, Simulated electric field (Re(E_x)) distributions of the reflected light for (V_t, V_b) for three different voltage combinations. **b**, Zero amplitude but similar phase as in **a**. **c**, The same amplitude as in **a** but opposite phase. Insets: magnified views of the electric field intensity ($|E_x|^2+|E_z|^2$) inside the plasmonic nanoresonator, the carrier concentration and the resulting Re(ε_{ITO}) inside the 5-nm-thick ITO layer for three different applied biases. **d**, Constellation diagram showing evenly distributed 13 target reflection phasors (marked by ×) and the numerically calculated phasors (indicated by red circles) obtained from applying V_t and V_b. The reflection coefficients at I, II and III were produced by using the voltage combinations in **a**–**c**. The remaining four and six phasors along the inner and outer circles, respectively, were also generated by using the voltage-reflection mapping relationship (Methods). **e**, Constellation diagram showing 13 target phasors (marked by ×) and the experimentally obtained phasors (indicated by red circles) generated by applying V_t and V_b. The difference in the amplitudes between **d** and **e** may originate from limitations in the characterization set-up (Methods). **f**, Experimental demonstration of the phase-only modulation showing the continuous phase change from 0 to 360° while maintaining constant reflectivity. Slight variations in the reflectivity result from the effects of using a coarse voltage step of 0.5 V (Methods).

For $r_{target}=-0.08i$ at III, we further decreased r_{imag} by setting $V_t=-3.00$ V. Although the intensity distribution may appear to be similar to that in the inset of Fig. 3b, the upper interface entered deep depletion, which substantially increased Re(ε_{ITO}) at the upper interface (Fig. 3c insets). The resulting coefficient was $0.0004-0.0750i$. The reflected field exhibits a similar amplitude to that in Fig. 3a, but ~180° out of phase (Fig. 3c). Using this approach, we obtained the appropriate voltage combinations that produced the ten remaining reflection coefficients (Fig. 3d and Methods).

We also experimentally generated the 13 target coefficients (Fig. 3e and Methods). Most coefficients closely matched their target values, with three phasors (at 0° and 270° along the inner circle and at 135° along the outer circle) that exhibited noticeable discrepancies from their ideal targets possibly due to the large driving-voltage step size (0.5 V) (Methods). Using the coefficients from the outer circle of Fig. 3e, we also experimentally demonstrated a continuous phase sweep from 0 to 360° as we maintained a constant reflectivity (or amplitude), which demonstrated phase-only modulation (Fig. 3f). Such a result could not be achieved in previous studies that employed one-control-parameter approaches[17–19] (Supplementary Section 1 and Supplementary Fig. 1).

As it is resonance-based, the range of the wavelengths over which the nanoresonator array can provide over an 300° phase change is restricted to near-resonance wavelengths. The bandwidth was measured to be ~20 nm (Supplementary Section 7 and Supplementary Figs. 9–11).

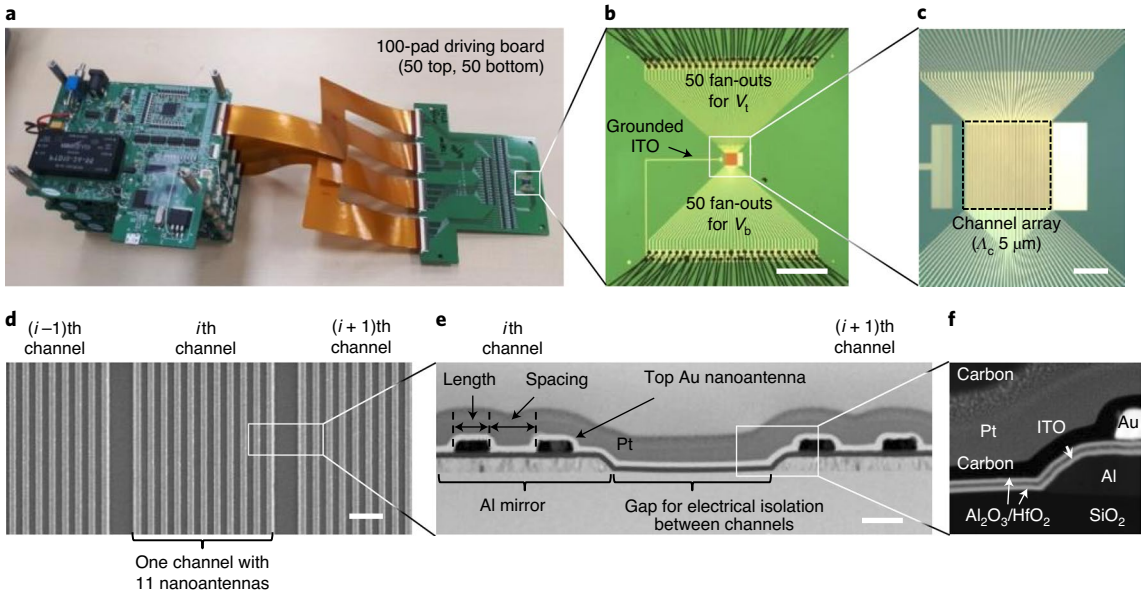

Fig. 4 | Active metasurface array with the driving electronics (metaphotonic SLM). a, Active metasurface array mounted on an electronics board capable of independently driving 100 channels for 50 V_t and 50 V_b terminals. **b**, Optical microscopy image of the active array at the centre of the fan-outs designed to provide individual connections for 50 V_t and 50 V_b terminals. Scale bar, 1 mm. **c**, Magnified view of the optical image of the active array located in the middle of the fan-outs with a size of 250 × 250 μm^2. For the dynamic wavefront manipulation, we defined a fundamental operating block called the channel with the period Λ_C of 5 μm. Scale bar, 100 μm. **d**, Scanning electron microscopy image showing one full and two partial channels. Each channel consists of a group of 11 nanoresonators. Scale bar, 1 μm. **e**, Transmission electron microscopy image showing the cross-sectional view of the region marked by the white box in **d**. The lateral gap between the two Al mirrors electrically isolates the two neighbouring channels. Scale bar, 200 nm. **f**, High-angle annular dark-field transmission electron microscopy image confirming the excellent step coverage on the appropriately sloped sidewall of an Al mirror that allows the thin ITO layer to be continuous (and grounded) throughout the entire array. This is crucial for the proper operation of the active array because charge modulations occur inside the ITO layer.

SLM for beam splitting and steering

To show the versatile ability for wavefront shaping, we fabricated the metaphotonic SLM with individually addressable channels. The driving electronics (Fig. 4a) provide 100 voltage-output terminals and independently control 50 top and 50 bottom gates of the metaphotonic SLM (Fig. 4b). The active array in the middle of the fan-outs (Fig. 4c) has 50 channels, each of which consists of a group of 11 nanoresonators (Fig. 4d). The cross-sectional view (Fig. 4e) clearly shows the gap that electrically isolates the two adjacent channels. The sidewalls of the Al mirrors were appropriately sloped (Fig. 4f), so that the thin 5 nm ITO layer remains continuous throughout the device (Supplementary Section 8 and Supplementary Figs. 12 and 13).

We first demonstrated beam splitting using the sinusoidal amplitude grating. Figure 5a shows the phase and reflectivity across each channel. The number of the channels per super cell or its period (Λ_{SC}) determines the splitting angle θ given by $\sin^{-1}(\lambda_0/\Lambda_{SC})$, where λ_0 is the free-space wavelength[2]. The beam image and intensity profiles are presented in Fig. 5b,c, respectively. Owing to the limited diffraction efficiency inherent to amplitude modulation, the zero-order beam has a higher intensity than the split beams highlighted in grey in the middle and bottom panels of Fig. 5c (Methods)[2].

We further improved the intensity of the intended first-order beam using a binary phase grating (Fig. 5d). The diffraction efficiencies of the zero- and first-order beams are given by $\eta_0 = |(r_1 + r_2)/2|^2$ and $\eta_1 = |(r_1 - r_2)/\pi|^2$, respectively, where r_1 and r_2 correspond to the two alternating complex reflection coefficients and η_j denotes the diffraction efficiency of the jth-order beam[2]. In Fig. 5e,f, the ratio η_1/η_0 gradually increases with increasing $\Delta\varphi$ and reaches its maximum value of 4.7 dB at $\Delta\varphi = 174°$. Previous work on active metasurfaces could not achieve $\eta_1 > \eta_0$ in the NIR due to insufficient $\Delta\varphi$ and/or non-uniform amplitudes[6,17,34].

We also demonstrated dynamic beam steering with a saw-tooth phase grating[2] (Fig. 5g). We show the far-field patterns of five selected steering angles in Fig. 5h and other cases in Supplementary Section 9 and Supplementary Figs. 14–16. The SMSR, defined as the intensity ratio between the main lobe and the highest side lobe[35], is a critical performance metric for applications, such as LiDAR, that must accurately distinguish objects from the background. We measured a high SMSR value of +2.7 dB (Fig. 5i and Supplementary Fig. 17). The SMSR can be further improved by minimizing the fabrication imperfection and the variation in amplitudes (Supplementary Section 10 and Supplementary Fig. 18).

To obtain the modulation speed of our device, we fabricated an identically structured test array with an active area sufficiently large (200 × 200 μm^2) for the probing beam through an objective lens to illuminate only the active area (Methods and Supplementary Fig. 19). The 3 dB cutoff frequency was 170 kHz. As the area of an individual channel was 1/32 of the area of the entire array, the channel's switching speed was estimated at 5.4 MHz (Supplementary Section 11 and Supplementary Fig. 20). The switching energy was 283 fJ μm^{-2} (Methods and Supplementary Table 1). The field of view of our device was ±7.7° (= $\sin^{-1}[\lambda_0/(2\Lambda_C)]$) (ref. [36]), and it could reach up to ±90° if we reduced the channel period down to 400 nm utilizing the same fabrication technologies as used to build our devices (Supplementary Section 12 and Supplementary Figs. 21 and 22).

The deflection efficiency η_{DE} is defined as the intensity of the main lobe normalized with respect to the sum of the background intensities ($\eta_1/(\sum\eta_j$ for all $j)$) (refs. [2,14]). Our active array exhibited η_{DE} values between 34 and 48% (Fig. 5i). The diffraction efficiency, defined as the intensity of the main lobe divided by the total input intensity, was approximately 1% because we chose to operate our

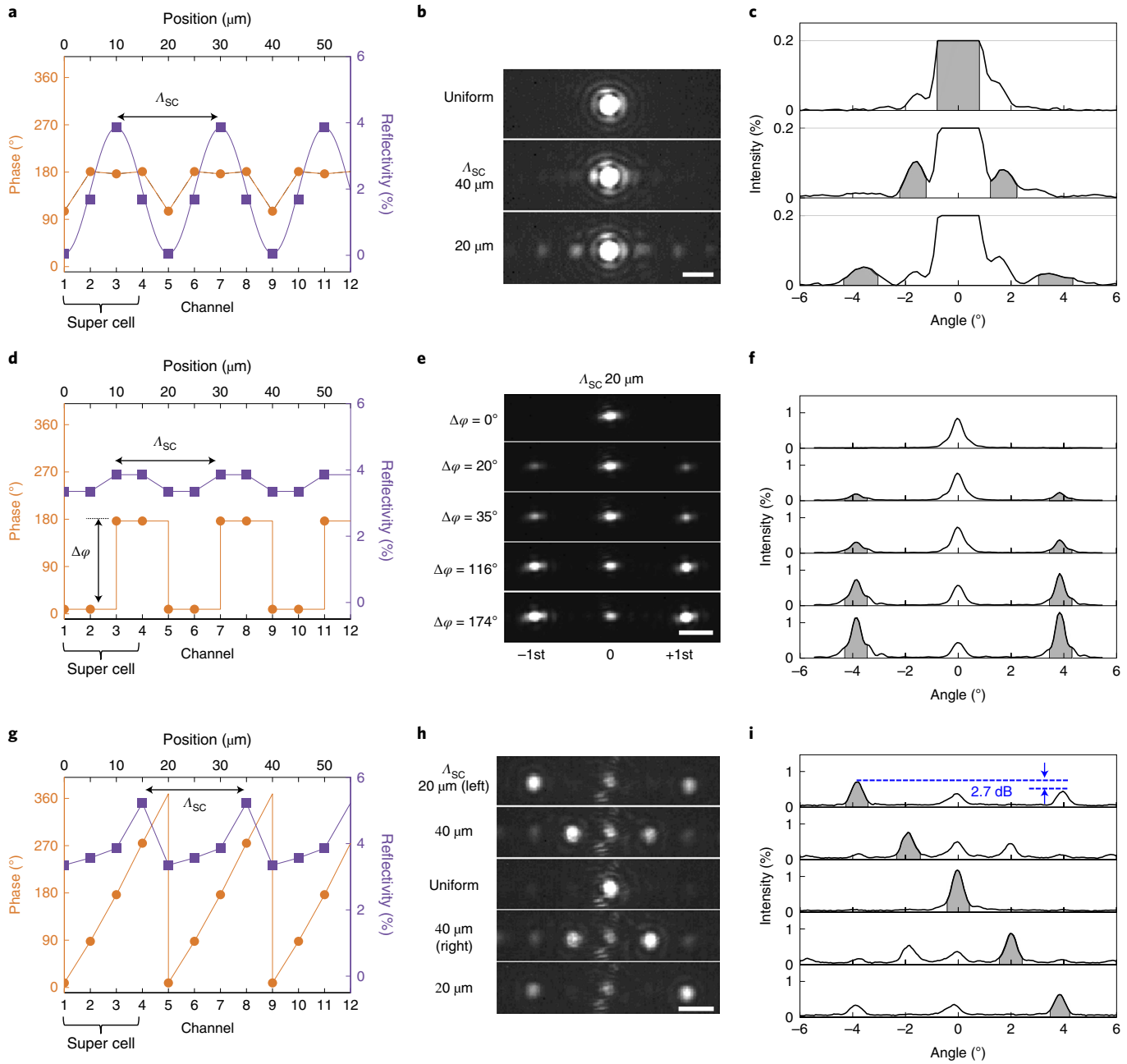

Fig. 5 | Beam splitting and steering using the metaphotonic SLM at 1.34 μm. a, Generation of the sinusoidal amplitude grating with the amplitude-only modulation for beam splitting. The reflectivity varies periodically across each channel, whereas the phase remains relatively constant. This periodicity is determined by the size of the operating unit called the super cell and, for this case, each super cell consists of four channels. **b**, Intensity profiles for three cases: 0° (top), ±1.92° for $\Lambda_{SC} = 40\,\mu m$ and ±3.84° for $\Lambda_{SC} = 20\,\mu m$. Scale bar, $0.03k_0$, where the wavenumber k_0 is given by $2\pi/\lambda_0$. **c**, The splitting angles determined by Λ_{SC} are ±1.92° (middle plot) and ±3.84° (bottom plot). **d**, Generation of the binary phase grating with the phase-only modulation for beam splitting. The phase gap is denoted by $\Delta\varphi$. **e**, Intensity profiles showing that as the phase gap $\Delta\varphi$ approaches 180°, the intensity of the zero-order beam (η_0) vanishes due to destructive interference, and that of the first-order beam (η_1) is maximized. Scale bar, $0.03k_0$. **f**, Intensity distribution showing the gradual increase of $\eta_{\pm1}/\eta_0$ to reach the maximum value at $\Delta\varphi \approx 180°$. **g**, Generation of the saw-tooth phase grating for beam steering. **h**, Intensity profiles for five steering angles of −3.84°, −1.92°, 0°, +1.92° and +3.84° showing linear movements of the focus beam. Scale bar, $0.03k_0$. **i**, Beam steering with an SMSR of +2.7 dB. All of the results shown in **a**–**i** were produced using the same device.

device at this efficiency to accomplish an independent modulation of the amplitude and phase over a 0–360° range with a high SMSR. The diffraction efficiency could be further improved by using insulating layers with a higher dielectric strength and constant[19] by employing transparent conducting oxides with a high mobility[37] and by reducing the channel period to remove higher order beams (Supplementary Section 13 and Supplementary Fig. 23).

Demonstrated use for LiDAR

Using the metaphotonic SLM, we demonstrated a proof-of-concept 3D LiDAR scan (Fig. 6a). The transmitter includes a 1,560 nm pulsed laser and our metaphotonic SLM redesigned and fabricated for operation at 1,560 nm (Methods). The receiver comprised a collector lens and an array of avalanche photodiodes (APDs). The object distance d was obtained by measuring the time delay τ

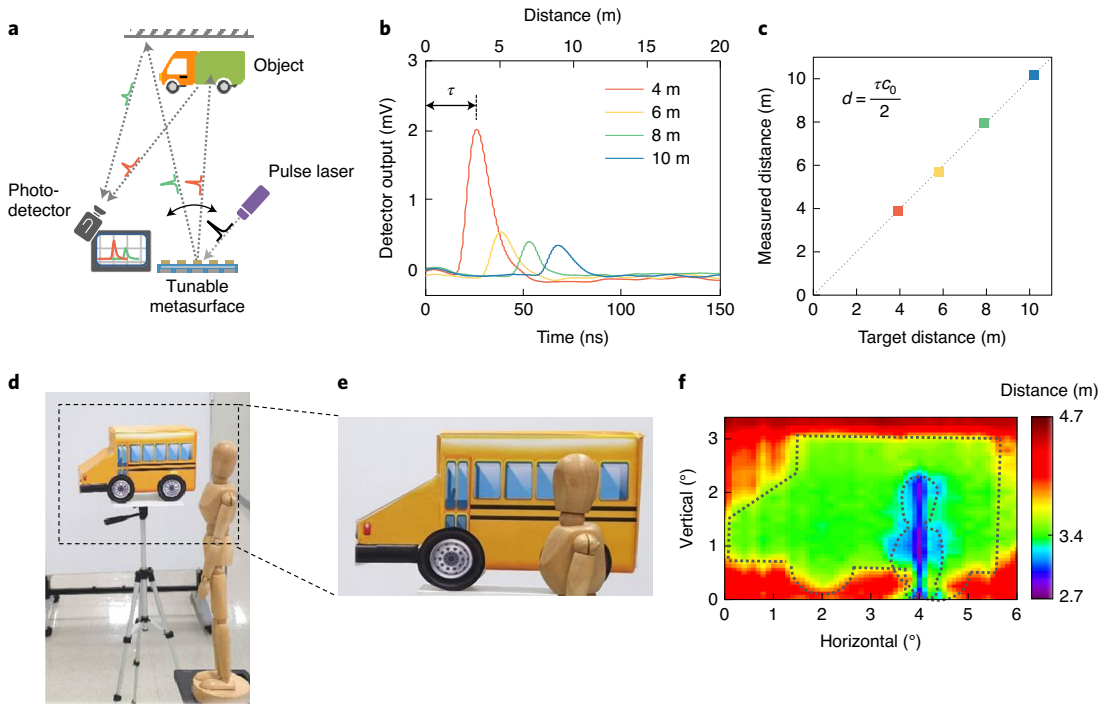

Fig. 6 | 3D LiDAR of an emulated street scene using the metaphotonic SLM at 1.56 µm. a, Schematic diagram of the 3D LiDAR experimental set-up. Pulses from the laser are incident on and reflected from the metaphotonic SLM. The steered pulses illuminate the objects, and an array of APDs captures the returning laser pulses and converts them into electrical signals to calculate the delays and the corresponding distances to the objects. Our active array scans horizontally, and hence we added a tilting stage for vertical scanning. **b**, Detector output as a function of flight time for the distances of 4, 6, 8 and 10 m. **c**, Time-of-flight measurements for distances up to 10 m: the measured time-of-flight was converted into the corresponding distance using equation (2). The accuracy, defined as the absolute difference between the actual and measured distances, was 4 cm for single-point measurements. **d**, Bird's eye view of the objects under scan: the scanned region is indicated by the dashed rectangular box. **e**, Magnified view of the scan region. **f**, 3D depth image produced using the metaphotonic SLM, which demonstrates the feasibility of the use of the metaphotonic SLM as the core scanning component in a LiDAR system. The scan angle range, angle step size and resolution are 6° (H) × 4° (V), 0.2° (H) × 0.2° (V) and 31 × 21 = 651, respectively, where H and V denotes the horizontal and vertical axes, respectively.

between the emission of the laser and its return to the APD array (Fig. 6b,c) (Methods):

$$d = \frac{\tau c_0}{2} \quad (2)$$

After a series of single-point measurements, we set the minimum acceptable signal-to-noise ratio at 10 dB and found 10 m as the maximum range (Fig. 6b and Methods).

For 3D range mapping, we emulated a street scene and scanned a human figure, a model car, and a screen placed in the order of increasing distance from the metaphotonic SLM (Fig. 6d and Methods). The distances to the human figure, the model car and the screen were 2.4, 3.4 and 4.7 m, respectively. Figure 6e,f shows the scanned region (Supplementary Movie 4) and the resulting depth map, respectively. We observed a good agreement between the measurements and the actual distances for all the targets except for an about 0.3 m distance error in the human figure. The distance to the screen defined the detection range of 4.7 m. The detection range and the accuracy could be further enhanced by improving the device efficiency and the SMSR and by optimizing transmitter and receiver optical configurations (Supplementary Section 14).

Conclusions

We have shown an ultrafast electrically tunable metaphotonic SLM and demonstrated full wavefront manipulation in the NIR regime. With an additional degree of freedom and the vectorial nature that allows the independent superposition of two input voltages, we accomplished independent modulation of the amplitude and phase over 360° (ref. [38]). The individually controllable metasurface array achieved a scan angle of 8°, SMSR of +2.7 dB, deflection efficiency over 34%, channel switching speed of 5.4 MHz and energy consumption of 283 fJ µm^{-2}. With the diffraction efficiency of 1% chosen for full wavefront modulation, we experimentally demonstrated a proof-of-concept LiDAR with a detection range up to 4.7 m.

An adaptation of well-established integrated-circuit technologies, such as an active matrix, can enable the realization of a large-scale 2D active metasurface array. We also expect that the proposed two-control-parameter approach can be realized in the visible range with the use of index-changing materials suitable for the visible part of the electromagnetic spectrum[6,22] (Supplementary Section 7 and Supplementary Figs. 10 and 11). Being all solid state, our device allows high-speed operation, robustness against mechanical impact or vibration, scalability and narrow beam divergence. With excellent semiconductor-process compatibility, our two-control-parameter approach and its hardware implementation could facilitate the development of practical and commercially viable SLMs.

Online content

Any methods, additional references, Nature Research reporting summaries, source data, extended data, supplementary information, acknowledgements, peer review information; details of author contributions and competing interests; and statements of data and code availability are available at https://doi.org/10.1038/s41565-020-00787-y.

Received: 12 November 2019; Accepted: 17 September 2020;
Published online: 26 October 2020

References

1. Savage, N. Digital spatial light modulators. *Nat. Photon.* **3**, 170–172 (2009).
2. Goodman, J. W. *Introduction to Fourier Optics Ch. 4* (McGraw-Hill, 1996).
3. Watts, C. M. et al. Terahertz compressive imaging with metamaterial spatial light modulators. *Nat. Photon.* **8**, 605–609 (2014).
4. Grilli, S. et al. Whole optical wavefields reconstruction by digital holography. *Opt. Express* **9**, 294–302 (2001).
5. Kim, Y. et al. Electrically tunable transmission-type beam deflector using liquid crystal with high angular resolution. *Appl. Opt.* **57**, 5090–5094 (2018).
6. Li, S.-Q. et al. Phase-only transmissive spatial light modulator based on tunable dielectric metasurface. *Science* **364**, 1087–1090 (2019).
7. Wang, Y. et al. 2D broadband beamsteering with large-scale MEMS optical phased array. *Optica* **6**, 557–562 (2019).
8. Yang, W. et al. High speed optical phased array using high contrast grating all-pass filters. *Opt. Express* **22**, 20038–20044 (2014).
9. Zheludev, N. I. & Kivshar, Y. S. From metamaterials to metadevices. *Nat. Mater.* **11**, 917–924 (2012).
10. Kildishev, A. V., Boltasseva, A. & Shalaev, V. M. Planar photonics with metasurfaces. *Science* **339**, 1232009 (2013).
11. Arbabi, A., Horie, Y., Bagheri, M. & Faraon, A. Dielectric metasurfaces for complete control of phase and polarization with subwavelength spatial resolution and high transmission. *Nat. Nanotechnol.* **10**, 937–943 (2015).
12. Yu, N. et al. Light propagation with phase discontinuities: generalized laws of reflection and refraction. *Science* **334**, 333–337 (2011).
13. Pors, A., Nielsen, M. G., Eriksen, R. L. & Bozhevolnyi, S. I. Broadband focusing flat mirrors based on plasmonic gradient metasurfaces. *Nano Lett.* **13**, 829–834 (2013).
14. Lin, D., Fan, P., Hasman, E. & Brongersma, M. L. Dielectric gradient metasurface optical elements. *Science* **345**, 298–302 (2014).
15. Shaltout, A. M., Shalaev, V. M. & Brongersma, M. L. Spatiotemporal light control with active metasurfaces. *Science* **364**, 648 (2019).
16. Park, J., Kang, J.-H., Liu, X. & Brongersma, M. L. Electrically tunable epsilon-near-zero (ENZ) metafilm absorbers. *Sci. Rep.* **5**, 15754 (2015).
17. Huang, Y.-W. et al. Gate-tunable conducting oxide metasurfaces. *Nano Lett.* **16**, 5319–5325 (2016).
18. Park, J., Kang, J.-H., Kim, S. J., Liu, X. & Brongersma, M. L. Dynamic reflection phase and polarization control in metasurfaces. *Nano Lett.* **17**, 407–413 (2017).
19. Shirmanesh, G., Sokhoyan, R., Pala, R. A. & Atwater, H. A. Dual-gated active metasurface at 1550 nm with wide (>300°) phase tunability. *Nano Lett.* **18**, 2957–2963 (2018).
20. Karvounis, A., Gholipour, B., MacDonald, K. F. & Zheludev, Z. I. All-dielectric phase-change reconfigurable metasurface. *Appl. Phys. Lett.* **109**, 051103 (2016).
21. Hosseini, P., Wright, C. D. & Bhaskaran, H. An optoelectronic framework enabled by low-dimensional phase-change films. *Nature* **511**, 206–211 (2014).
22. Tittl, A. et al. A switchable mid-infrared plasmonic perfect absorber with multispectral thermal imaging capability. *Adv. Mater.* **27**, 4597–4603 (2015).
23. Lee, J. et al. Giant nonlinear response from plasmonic metasurfaces coupled to intersubband transitions. *Nature* **511**, 65–69 (2014).
24. Jun, Y. C. et al. Epsilon-near-zero strong coupling in metamaterial–semiconductor hybrid structures. *Nano Lett.* **13**, 5391–5396 (2013).
25. Yao, Y. et al. Electrically tunable metasurface perfect absorbers for ultrathin mid-infrared optical modulators. *Nano Lett.* **14**, 6526–6532 (2014).
26. Dabidian, N. et al. Electrical switching of infrared light using graphene integration with plasmonic Fano resonant metasurfaces. *ACS Photon.* **2**, 216–227 (2015).
27. Sherrott, M. C. et al. Experimental demonstration of >230° phase modulation in gate-tunable graphene–gold reconfigurable mid-infrared metasurfaces. *Nano Lett.* **17**, 3027–3034 (2017).
28. van de Groep, J. et al. Exciton resonance tuning of an atomically thin lens. *Nat. Photon.* **14**, 426–430 (2020).
29. Holsteen, A. L., Cihan, A. F. & Brongersma, M. L. Temporal color mixing and dynamic beam shaping with silicon metasurfaces. *Science* **365**, 257–260 (2019).
30. Shaltout, A. M. et al. Spatiotemporal light control with frequency-gradient metasurfaces. *Science* **365**, 374–377 (2019).
31. Jia, S. L., Wan, X., Su, P., Zhao, Y. J. & Cui, T. J. Broadband metasurface for independent control of reflected amplitude and phase. *AIP Adv.* **6**, 045024 (2016).
32. Lee, G.-Y. et al. Complete amplitude and phase control of light using broadband holographic metasurfaces. *Nanoscale* **10**, 4237–4245 (2018).
33. Haus, H. A. *Waves and Fields in Optoelectronics* (Prentice-Hall, 1984).
34. Horie, Y., Arbabi, A., Arbabi, E., Kamali, S. M. & Faraon, A. High-speed, phase-dominant spatial light modulation with silicon-based active resonant antennas. *ACS Photon.* **8**, 1711–1717 (2018).
35. Komljenovic, T., Helkey, R., Coldren, L. & Bowers, J. E. Sparse aperiodic arrays for optical beam forming and LiDAR. *Opt. Express* **25**, 2511–2528 (2017).
36. Jiang, Q., Jin, G. & Cao, L. When metasurface meets hologram: principle and advances. *Adv. Opt. Photon.* **11**, 518–576 (2019).
37. Lin, M.-L. et al. High mobility transparent conductive Al-doped ZnO thin films by atomic layer deposition. *J. Alloys Compd.* **727**, 565–571 (2017).
38. Neshev, D. & Aharonovich, I. Optical metasurfaces: new generation building blocks for multi-functional optics. *Light Sci. Appl.* **7**, 58 (2018).

Methods

Modelling and simulation. In Fig. 2a–c, the values for the parameters in equation (1) were chosen to help illustrate the cause-and-effect relationship of the spectral shifts and the transitions of the coupling dynamics. We set the parameters γ_{rad}, γ_{abs} and λ_r to 1.7×10^{14} rad s^{-1}, 1.4×10^{14} rad s^{-1} and 1.3 μm, respectively, for no-bias, to 1.7×10^{14} rad s^{-1}, 2.0×10^{14} rad s^{-1} and 1.2 μm, respectively, for accumulation and to 1.7×10^{14} rad s^{-1}, 1.2×10^{14} rad s^{-1} and 1.4 μm), respectively, for depletion.

We chose the gate dielectric material that can maximize the charge-carrier concentration under the application of an external electrical bias. The HfO_2 layer was found to be more advantageous due to its large d.c. permittivity (18) and high dielectric strength (~3.5 MV cm^{-1}). The Al_2O_3 layer was used to promote adhesion. The thickness of the ITO film should be kept as thin as possible to minimize the quasi-neutral region between the two modulated regions (accumulation and/or depletion layers) at the interfaces and, simultaneously, the consistency and uniformity of the ITO film must be preserved. The smallest thickness for which the consistent and uniform ITO film can be deposited using the currently available d.c. sputtering technique was approximately 5 nm.

The geometry of the nanoresonators was defined by their length and the spacing or the edge-to-edge distance between two neighbouring nanoantennas. The length determines the resonance wavelength and the spacing governs the coupling dynamics. For the full-field simulation, the antenna length and the spacing were chosen as 175 and 195 nm (the period of 370 nm), respectively, to have a resonance wavelength of 1.30 μm and operate in the near-critical-coupling regime (Supplementary Section 5 and Supplementary Figs. 6 and 7). The two-control-parameter approach can easily be adapted for use in other spectral ranges, different gate dielectric materials of different thicknesses and/or nanoantennas of different shapes or forms, such as the fishbone or rectangular shapes.

The carrier density profile in the ITO film was calculated using the commercially available Synopsys Technology Computer-Aided Design software. The nanoresonator was modelled as a stacked structure that consisted of an Al mirror–Al_2O_3/HfO_2 (gate dielectric)–ITO (active layer)–Al_2O_3/HfO_2 (gate dielectric)–Au antenna. The ITO film was grounded and various voltage combinations were applied to the nanoantennas and mirrors. The background carrier density n_{bg} was experimentally measured as 4.0×10^{20} cm^{-3} and was used in the Synopsys Technology Computer-Aided Design simulation. For simplicity, we assumed that we could ignore the variations of the carrier profile n as a function of the position at the vicinity of the antenna edges. Only two 1D carrier profiles were extracted along the lines below and outside the Au antenna. To describe the varying carrier profile in finite-difference time-domain simulations, we modelled the 5-nm-thick ITO layer as a vertical stack of 0.025-nm-thick multilayers based on the Drude model, in which each layer had a slightly different carrier concentration from the layers above and/or below, and the plasma frequency of each layer was estimated from the carrier density profile $\varepsilon_{ITO}=\varepsilon_{inf}-\omega_P^2/[\omega(\omega-i\Gamma)]$, where $\omega_P^2=(ne^2)/(m_e^*\varepsilon_0)$ (ref. [39]). The effective mass m_e^*, scattering rate Γ and static permittivity ε_{inf} used in the finite-difference time-domain simulation were $0.35\times m_e$, 1.0×10^{14} rad s^{-1} and 3.9, respectively, where e is the charge of the electron, m_e is the electron mass and ε_0 is the free-space electric permittivity. For these simulations, we assumed a time-harmonic electromagnetic field given by $\exp[i(\omega t-\mathbf{k}\cdot\mathbf{x})]$, where ω is the angular frequency, t is the time, $\mathbf{k}$ is the wavevector and $\mathbf{x}$ is the space coordinate. The indices of refraction of the metals (Au and Al) were adopted from the literature[40]. The refractive index of the HfO_2 gate dielectric was empirically obtained as 1.91 and that of Al_2O_3 was set to 1.66.

For the generation of the 13 points on the constellation diagram, the applied bias combinations (V_t, V_b) were (0.50 V, 4.65 V) for the origin; (2.00 V, 3.60 V), (2.75 V, 3.60 V), (3.25 V, 3.20 V), (2.25 V, 5.15 V), (1.75, 6.00 V), (−2.00 V, 5.10 V), (−3.00 V, 4.55 V) and (0.00 V, 4.00 V) for the 8 points along the outer circle with phase values that varied from 0° to 315° at a step size of 45° in the anticlockwise direction and (1.00 V, 4.25 V), (1.75 V, 4.60 V), (0.75 V, 5,00 V) and (−1.25 V, 4.60 V) for the 4 points along the inner circle with phase values that varied from 0° to 270° at a step size of 90° in the anticlockwise direction.

The switching energy per unit area was 283 fJ μm^{-2}, as calculated based on the capacitor storage energy $(1/2)\times CV^2\times2$, where C and V are the capacitance and the driving voltage, respectively. The capacitance of each channel was obtained considering the d.c. permittivity values of 18 and 9 for the 7-nm-thick HfO_2 and 1-nm-thick Al_2O_3 layers, respectively.

Fabrication. The 70-nm-thick Nd-doped Al layer was formed by sputtering on a Si substrate coated with an SiO_2 insulating layer. The gaps between the neighbouring channels were patterned by photolithography followed by dry etching. The lower insulating layer composed of Al_2O_3(1 nm)/HfO_2(7 nm) was deposited on top of the Al layer by atomic layer deposition. The 5-nm-thick ITO layer that served as the carrier-modulation layer was formed by d.c. magnetron sputtering. Then, the upper insulating layer was deposited on top of the ITO layer by atomic layer deposition. Finally, the 50-nm-thick Au antennas with a 5-nm-thick Cr-adhesion layer were fabricated by electron-beam lithography and electron-beam evaporation followed by a standard lift-off process. The Au antenna dimensions were adjusted slightly from the simulation results to cover the origin in the phasor diagram—an antenna length and spacing of 185 and 215 nm, respectively, which corresponded to the period of 400 nm.

Characterization of the reflection properties. The reflection spectrum of the metasurface was obtained using a broadband light source and an optical spectrum analyser (Yokogawa, AQ6370C). An NIR light source was incident on the device through a polarizer and was focused on the metasurface region, and the beam was reflected back and coupled to the optical spectrum analyser. By comparing the measured beam intensity from the nanoantenna region with the reference beam from the mirror region, the reflection spectrum was obtained. To improve the accuracy of the reflectivity measurements, it is important to exclude the effects of two electric field components that do not interact with the nanoresonator: one is the reflected beam from the reference mirror and the other is the electric field parallel to the nanoantennas (y coordinate in Fig. 1b). To illuminate only the active area of the nanoresonator array, we used an objective lens with a numerical aperture of 0.42 (Mitutoyo, M Plan Apo 20×). The angle of the polarizer was carefully adjusted to pass only the electric field perpendicular to the nanoantennas. The amplitude discrepancy in the amplitudes of the reflection coefficients between the simulation (Fig. 3d) and the measurement (Fig. 3e) may originate from unwanted electric field components that did not completely become extinguished.

The reflection phase-measurement system was based on a Michelson interferometer (Supplementary Section 15 and Supplementary Figs. 24–26). A coherent NIR light source (Keysight, 8164B and 81600B) with a very short spectral width (1 nm) was incident on the nanoantenna array through a beam splitter. The beam reflected from the nanoantenna array interfered with that from the reference mirror. The intensity and alignment of the beams from the two paths were adjusted to generate vertical fringes that were captured using an infrared camera (Aval, ABA-003IR-GE). We extracted the phase information from the captured fringes.

The phasor diagram was produced by using both the amplitude and phase information at each wavelength (Supplementary Section 16 and Supplementary Fig. 27). The far-field intensity profile at the Fourier plane was obtained using an infrared camera and a 4-f system at a wavelength of 1.34 μm (Supplementary Section 17 and Supplementary Fig. 28).

During the characterization, the current level of the device remained below 200 pA. Thus, there was no noticeable leakage-current issue for our device, and we did not observe any thermal drift that resulted from the leakage current (Supplementary Fig. 29).

Characterization of the proof-of-concept LiDAR. For the proof-of-concept LiDAR demonstration, a pulsed laser (Connet Laser Technology, CoLID-1) with a wavelength of 1.56 μm, pulse width of 10 ns and repetition rate of 10 kHz was used (duty cycle, 1/10^4). To change the operating wavelength of the metasurface from 1.34 to 1.56 μm, the metasurface design was slightly modified. We used 1-nm-thick Al_2O_3 and 11-nm-thick HfO_2 for the insulating layers. The length and spacing of the antenna were 210 and 110 nm, respectively, which corresponded to a period of 320 nm. A polarizer, an iris and collimation optics were used to illuminate the device area, and the peak and average powers incident on the device were 85 W and 85 mW, respectively. This power level is on a par with typical values observed in commercial LiDAR systems, for example, Velodyne HDL-64E, which uses a 75 W laser at a wavelength of 905 nm. The peak and average powers in the steered beam were approximately 850 mW and 850 μW, respectively, which is equivalent to an energy density of 85 μJ cm^{-2} and thus satisfies the eye-safety-level requirements: the maximum permissible exposure at a wavelength of 1.56 μm is 1 J cm^{-2} according to International Electrotechnical Commission 60825-1[41]. For the single-point measurement in Fig. 6b,c, we fixed the beam steering angle by using a binary phase grating with a Λ_{SC} of 10 μm to utilize the largest SMSR and employed an APD (Thorlabs, APD430C/M) with a high sensitivity of 18 A W^{-1} but a small aperture diameter of 0.2 mm.

For the 3D range mapping in Fig. 6f, which consists of a model car and a human figure (AA3012, MacPherson's), it was necessary to use an APD array because the reflected beams from different angles were focused through a lens on the detector plane with lateral shifts[39]. We thus used a 16×5 APD array (Wooriro, Inc.), which has a sensitivity of 2.5 A W^{-1}, aperture dimensions of 9.6×3.0 mm^2 and pixel dimensions of 600×600 μm^2. To generate high-quality scan images, we limited the horizontal and vertical scan angles to 6 and 4°, respectively. The signals from the APD array were captured and processed using a high bandwidth oscilloscope (Teledyne LeCroy Inc., 760zi-A 6 GHz) with a sampling rate of 40 GS s^{-1}.

Data availability

The data that support the plots within this paper and other findings of this study are available from the corresponding authors upon reasonable request. Source data are provided with this paper.

Code availability

All the scripts are available from the corresponding author upon reasonable request.

References

39. Saleh, B. E. A. & Teich, M. C. *Fundamentals of Photonics 2nd edn* (Wiley-Interscience, 2007).

40. Palik, E. D. *Handbook of Optical Constants of Solids Vol. 1* (Academic Press, 1997).
41. *Safety of Laser Products—Part 1: Equipment Classification and Requirements 60825-1* edition 1.2 Table 6 (International Electrotechnical Commission, 2001).

Acknowledgements

We appreciate the support of N. Han, J.-Y. Hwang, B. J. Kim, M. K. Lee, D.-K. Nam, Y.-H. Cho, S.-K. Cho, G. Kim, H.-E. Lee, B. I. Yoo, S. Rhee, J.-J. Han and Y.-C. Cho. We thank H. A. Atwater for insightful discussions.

Author contributions

J.P. and J. Kyoung conceived the initial idea. J.P., B.G.J., S.I.K., D.L. and S.H.S. expanded and developed the concept. J.P. and C.S. conducted theoretical modelling. B.G.J. and S.I.K. designed the experiments. S.I.K. and C.B.L. characterized the optical properties of the device. T.O. developed the driving board. S.I.K., K.-Y.Y. and Y.-Y.P. fabricated the device. S.K. conducted and analysed the modulation bandwidth experiment. B.G.J., D.L. and J.J. established the transmitter module for the ranging experiment. J.L., I.H. and K.H. implemented the receiver module for the ranging experiment. J. Kim, H.C., B.L.C., M.L.B. and S.-W.H. supervised the project. All the authors contributed to the manuscript preparation. H.C. and J.P. revised the manuscript.

Competing interests

J.P., J. Kyoung, S.I.K., C.S., B.G.J. and B.L.C. are inventors on US patent 10,670,941 held and submitted by Samsung Electronics that covers the use of the two-control-parameter approach for active wavefront manipulation and control. The authors declare no other competing interests.

Additional information

Extended data is available for this paper at https://doi.org/10.1038/s41565-020-00787-y.

Supplementary information is available for this paper at https://doi.org/10.1038/s41565-020-00787-y.

Correspondence and requests for materials should be addressed to J.P., H.C. or B.L.C.

Peer review information *Nature Nanotechnology* thanks Luke Sweatlock, Jason Valentine and the other, anonymous, reviewer(s) for their contribution to the peer review of this work.

Reprints and permissions information is available at www.nature.com/reprints.

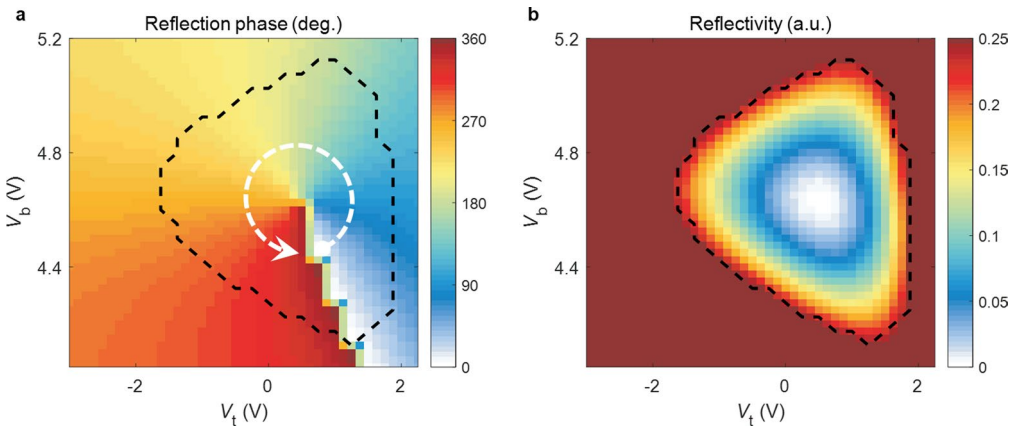

Extended Data Fig. 1 | Complete coverage of the phase and the amplitude (reflectivity) for arbitrary generation of a desired reflection coefficient. **a**, Reflected phase map on the color scale obtained by running full field simulation with the conditions given in Fig. 2e and varying V_t from −3 V to 2.25 V and V_b from 4.05 V to 5.2 V: if (V_t, V_b) = (0.5 V, 4.6 V) is considered approximately as a reference origin, the result shows the full 360° phase coverage for every concentric ring, for example, along the loop made by the white dashed circular arrow, within the region of interest indicated by the black dashed boundary. **b**, Reflectivity map on the color scale for the same voltage ranges: every pseudo-circular annulus (or concentric ring) formed by a single color represents an identical reflectivity. When each of these annuli is superposed on top of the reflection-phase map shown in **a**, it becomes clear that for every amplitude, it is possible to find a voltage combination (V_t, V_b) that leads to any desired phase between 0 and 360°, allowing arbitrary generation of a desired reflection coefficient.

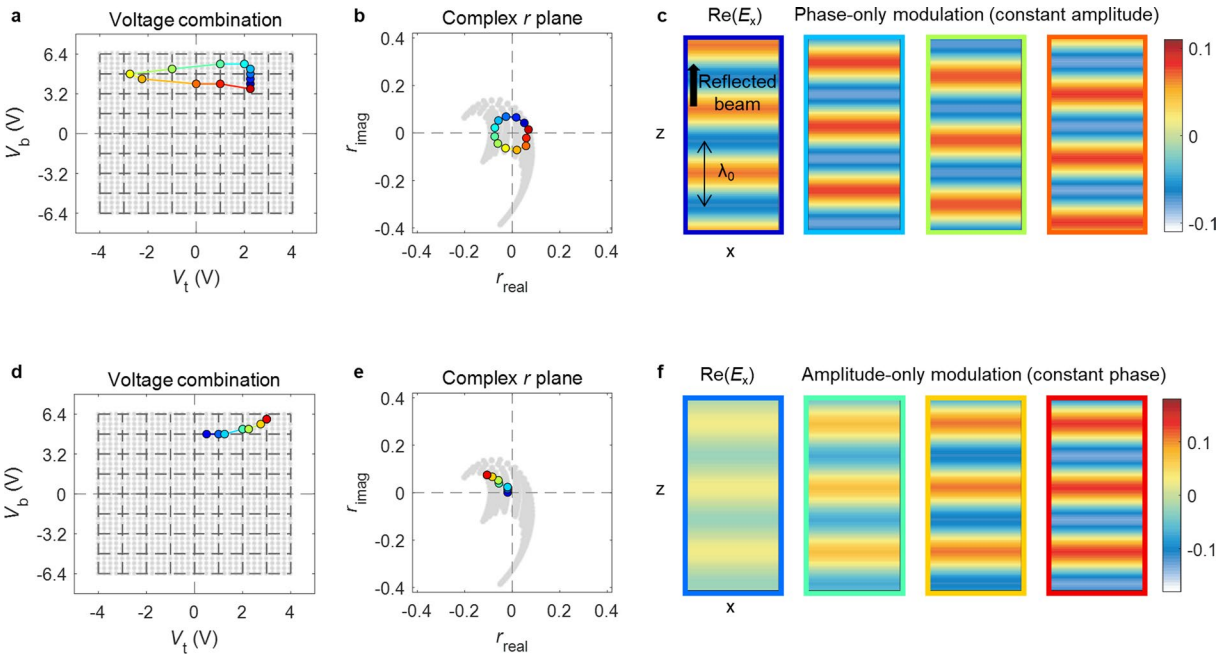

Extended Data Fig. 2 | Phase-only and amplitude-only modulations using the two-control-parameter approach. a, A set of voltage combinations selected for the phase-only modulation or the constant-amplitude and 0–360° phase shift. **b**, Trajectory of the reflection coefficients for the phase-only modulation: it makes a circular ring around the origin, showing the 0–360° phase shift. **c**, Real part of the electrical field along the *x*-axis, showing the gradual phase shift that eventually builds up to 360°. **d**, A set of voltage combinations selected for the amplitude-only modulation. **e**, Corresponding phasor trajectory that clearly exhibits the constant phase while varying the amplitude from 0 to its full value. **f**, Real part of the electrical field along the *x*-axis, showing no change in the phase while the intensity gradually increases.